JGR Atmospheres

RESEARCH ARTICLE
10.1029/2018JD029365

United States Heat Wave Frequency and Arctic Ocean Marginal Sea Ice Variability

Dagmar Budikova[1], **Trent W. Ford**[2], **and Thomas J. Ballinger**[3]

[1]Department of Geography, Geology, and the Environment, Illinois State University, Normal, IL, USA, [2]Department of Geography and Environmental Resources, Southern Illinois University, Carbondale, IL, USA, [3]Department of Geography, Texas State University, San Marcos, TX, USA

Key Points:
- Low summer sea ice in Hudson Bay is statistically linked to an increased frequency of summer U.S. heat waves
- Extreme heat waves are more common across southern Plains; oppressive heat waves are more common in the Southeast
- Heat wave flavor is shaped by local surface-atmospheric conditions

Supporting Information:
- Supporting Information S1

Correspondence to:
D. Budikova,
dbudiko@ilstu.edu

Citation:
Budikova, D., Ford, T. W., & Ballinger, T. J. (2019). United States heat wave frequency and Arctic Ocean marginal sea ice variability. *Journal of Geophysical Research: Atmospheres*, *124*, 6247–6264. https://doi.org/10.1029/2018JD029365

Received 19 JUL 2018
Accepted 26 APR 2019
Accepted article online 17 MAY 2019
Published online 24 JUN 2019

Abstract Recent studies point to a significant rise in the number of summer extreme weather events that correspond with the presence of amplified, quasistationary midtropospheric planetary waves, weakened atmospheric circulation in the Northern Hemisphere, and coincide with reduced summer Arctic sea ice cover. This study explores potential connections between 1979 and 2016 summer heat wave frequency across the USA and regional Arctic sea ice extent (SIE) in various Arctic basins. Most notable SIE interannual relationships exist across the southern Plains and southeastern US during low Hudson Bay summer SIE. Locally increased frequencies of summer heat waves coincide with unseasonably warm conditions developed and sustained by the presence of an omega blocking pattern situated over the southern US throughout summer. The block appears following anomalous atmospheric warming and reduced mean zonal winds observed throughout spring (March–May) over northeastern Canada, the northwestern Atlantic basin, and Greenland. Spring preconditioning of summer ice melt is favored by the presence of strong negative phase of the North Atlantic Oscillation and positive Greenland Blocking Index. Summer synoptic flow related to Hudson Bay ice melt over North America appears to be influenced by the background state of atmospheric variability, namely, the positive phase of the Atlantic Multidecadal Oscillation. Antecedent local humidity, soil moisture, and precipitation conditions are shown to influence the "flavor" of the heat waves, which are more likely to be oppressive in the southeastern US and extreme across the southern Plains during summers experiencing low Hudson SIE.

1. Introduction

Pan-Arctic warming over the last several decades has resulted in a rapid decline in sea ice thickness, extent, and volume (Schweiger et al., 2011; Schweiger & Lindsay, 2015; Screen & Simmonds, 2010). September minimum sea ice extent (SIE) decreased at an estimated 13×10^5 km^2 per decade between 1997 and 2014 (Serreze & Stroeve, 2015) and has been connected to reductions in the Northern Hemisphere (NH) meridional near-surface air temperature gradient and overall increased geopotential heights over the Arctic region (e.g., Cohen et al., 2014). The spatial pattern and magnitude of ice melt have been shown to drive a local atmospheric warming response due to upward turbulent heat fluxes that dilate geopotential heights aloft and exert downstream/lower latitude impacts by increasing the amplitude of long-wave circulation patterns (Ballinger & Sheridan, 2015; Francis & Vavrus, 2015; McKenna et al., 2018). The largest reductions in Arctic-midlatitude temperature gradients have been observed in boreal summer (Walsh, 2014) that have further resulted in a weakening of zonal winds across the NH during this season (Coumou et al., 2015).

Consideration of temporal trends in pan-Arctic SIE and cover has proven important when investigating NH circulation pattern modulations and resultant spatial patterns in extreme weather events. Recent tropospheric warming and sea ice decline have not been uniformed across the entire Arctic basin; as expected, the greatest surface warming has been reported along the southern marginal seas including those bordering northeastern Canada and Greenland (Ding et al., 2014). For instance, the 1979–2006 annual average sea ice concentration trend in the Hudson Bay (HB) area has been among the highest magnitude in the Arctic, recorded at −19.5% per decade (Parkinson & Cavalieri, 2008; Tivy et al., 2011) compared to the pan-Arctic decline of 3%–4% per decade (Parkinson & Cavalieri, 2008) during the same period.

Concurrent with the recent Arctic sea ice decline has been an increase in the incidence, severity, and duration of extreme summer weather events across many regions of the NH, including extreme hot days

and heat waves across the USA (Della-Marta et al., 2007; Diffenbaugh et al., 2007; Perkins et al., 2012; Schoof et al., 2015). Schoof et al. (2017) note that central US has been experiencing significant increases in both extreme (i.e., high temperature and low humidity) and oppressive (i.e., high temperature and high humidity) heat waves over the past 30 years. Increased incidence of North American (NA) summer extreme heat has been linked to concurrent amplification of quasistationary, midtropospheric planetary waves (Coumou et al., 2014; Mann et al., 2017; Petoukhov et al., 2013; Screen & Simmonds, 2014).

Significant challenges surround our ability to establish physical linkages between extreme weather events in the middle latitudes and cryospheric conditions in the Arctic. Areas of intermittent boundary forcing and corresponding polar jet stream behaviors (i.e., a ridge over an anomalously warm portion of the Arctic Ocean and corresponding trough to the south and east bringing cold air into the midlatitudes), for instance, include key mechanisms in establishing these connections (Cohen et al., 2018; Vihma, 2014). Rossby wave and resonance theories have been used to argue that Arctic sea ice decline and Arctic warming can lead to NH atmospheric flow modifications with a potential for increased persistence and blocking events in the middle latitudes via a weakening of the poleward thermal gradient, mean zonal winds and thermal winds, reduction in total atmospheric kinetic energy, and an increase in the amplification of quasistationary wave numbers 6–8 (Coumou et al., 2015, 2017; Francis & Vavrus, 2012, 2015; Tang et al., 2013). These alterations provide more conducive environments for the development of summertime extreme weather events across the NH midlatitudes (Budikova & Chechi, 2016; Budikova et al., 2017; Coumou et al., 2014; Screen et al., 2015). In recent decades, low summer sea ice has been associated with the negative phase of the North Atlantic Oscillation (NAO) with increased (decreased) upper-level geopotential heights (zonal wind speeds) across the polar cap and a northward shift in the subpolar jet stream, leading to increased ridging and southerly advection of warm air from the subtropics (Budikova & Chechi, 2016; Francis & Vavrus, 2015; Mann et al., 2017; Schubert et al., 2011).

Middle latitude weather responses since the 1990s have been associated with regional sea ice forcing on atmospheric circulation (e.g., Overland, 2016; Screen, 2017; Screen & Francis, 2016; Shepherd, 2016). Others point out that the severity of extreme weather events, for instance, may be modified or amplified by regional Arctic thermodynamic influences on the large-scale atmospheric circulation (Overland, 2016; Overland & Wang, 2018). In a recent state-of-science report, Cohen et al. (2018) recognize that the Arctic-to-middle latitude linkages may be conditional on the background state of the hemispheric weather patterns and manifest themselves regionally on timescales of weeks to a few months. They propose that future work establishing linkages from the Arctic to the middle latitudes ought to recognize interactions between internal climatic variation and the global state of sea surface temperature (SST) forcings.

Arctic summer warming and sea ice loss have been linked to U.S. midlatitude summer temperature extremes (Budikova & Chechi, 2016). Heat wave literature, particularly studies, focused on the physical mechanisms driving onset and intensity traditionally focus on the sensible heat contribution to atmospheric heat content through analysis of maximum temperature (Diffenbaugh & Ashfaq, 2010; Mueller & Seneviratne, 2012; Oswald & Rood, 2014; Russo et al., 2014). However, recent studies highlight the increasingly important role of atmospheric humidity during heat waves and societal vulnerability to these events (Mitchell et al., 2016; Pal & Eltahir, 2016; Schär, 2016); the nature of heat events is dependent on local soil moisture availability and antecedent precipitation conditions (Ford & Schoof, 2017). Specifically, near-surface humidity conditions during periods of elevated temperatures can result in dramatically different human health outcomes (Anderson & Bell, 2009; Davis et al., 2016; Kunkel et al., 1996). Accordingly, numerous studies have augmented temperature-based heat wave descriptions with metrics that are sensitive to humidity, such as dew point temperature and wet bulb temperature (Bentley & Stallins, 2008; Pal & Eltahir, 2016). Pielke et al. (2004) recommend moist static energy to represent total atmospheric heat content, as it accounts for both temperature and moisture energy contributions. Moist static energy is defined such that

$$H = C_p\mathrm{T} + L_v\mathrm{q}, \tag{1}$$

where C_p is the specific heat of air at constant pressure (J/kg/°C), T is air temperature (°C), L_v is the latent heat of vaporization (J/kg), and q is specific humidity (kg/kg). Division of H by C_p gives equivalent temperature (T_E):

$$T_E = \frac{H}{C_p} = T + \frac{L_v q}{C_p}, \tag{2}$$

which is expressed in units of °C and practically represents the air temperature if all water vapor is condensed and the resulting latent energy is used to heat the air parcel. In this study, we distinguish oppressive heat waves (i.e., elevated temperature and humidity) from extreme heat waves (i.e., elevated temperature only) and analyze the two separately. Extreme and oppressive heat events across the USA are represented using daily values of maximum temperature (T_{MAX}) and T_E, respectively.

Arctic warming is partially attributable to sea ice decline with two-way effects on ridge-trough jet stream patterns that may influence middle latitude weather, including the incidence of extreme weather events (e.g., Budikova et al., 2017; Ding et al., 2017; Francis, 2017; Tang et al., 2014). Coincidence of dramatic SIE reductions with increased incidence of extreme summer temperatures in the midlatitudes over the last three to four decades may suggest potential physical mechanisms connecting the two and warrant an investigation of the relationships and dynamic linkages between the frequency of midlatitude extreme heat events and Arctic sea ice variability during the boreal summer (June–August). The primary objective of this study is to provide a robust exploration of the statistical relationships between Arctic marginal sea ice and U.S. summer heat wave frequencies. The approach utilizes observational records of summer Arctic SIE along with a multitude of variables depicting concurrent and antecedent surface, atmospheric, and oceanic fluctuations across the NH for the time period 1979–2016. The examined parameters include anomalies in surface moisture, evapotranspiration, precipitation, surface and atmospheric air temperature, sea level pressure, middle- and upper-level geopotential heights and winds, and SST. The work recognizes the latest theories and mechanisms related to Arctic-to-midlatitude weather linkages. For instance, sea ice rates of variability and change are not homogenous across the entire Arctic basin (Peng & Meier, 2017), and the spatial configuration of the polar jet stream may be altered by its geographic position with respect to Arctic open water (Francis et al., 2017; Koenigk et al., 2016; Overland & Wang, 2018; Screen, 2017), thereby modifying the frequency of extreme weather events such as boreal summer heat waves.

2. Data and Methods

2.1. Data

2.1.1. Atmospheric and Surface Conditions

Three hourly fields of air temperature (T, °C), dew point temperature (T_d, °C), and surface pressure (P, hPa) were obtained from the European Centre for Medium-Range Weather Forecasts interim reanalysis (ERA-Interim; Dee et al., 2011). ERA-Interim was selected to represent heat events in the USA because (1) it assimilates both near-surface temperature and humidity from surface weather stations, (2) it has sufficient horizontal resolution (0.75°) for representing mesoscale features such as heat waves, and (3) a recent analysis has demonstrated that ERA-Interim effectively reproduces observed heat wave characteristics and trends in the contiguous US (Schoof et al., 2017), meriting its use in this study. Daily maximum temperature (T_{MAX}, °C) and maximum equivalent temperature (T_E, °C) were computed from the 3-hr values of T, T_d, and P. Computing T_E, as demonstrated by equation (2), requires specific humidity (q, kg/kg), which is not included in the fields of variables produced by ERA-Interim. Therefore, we adopt the empirical relationship described by Bolton (1980) to calculate vapor pressure (e, hPa) from T_d:

$$e = 6.112\ \exp\left(\frac{17.67 T_d}{T_d + 243.5}\right) \tag{3}$$

We can then use e and P to estimate q such that

$$q = \frac{0.622e}{P - 0.378e} \tag{4}$$

Latent heat of vaporization (L_v) is then calculated as a function of T following the Priestley-Taylor method (e.g., Fall et al., 2010). Finally, the resulting terms are used to calculate daily T_E according to equation (2).

ERA-Interim fields are also used to characterize atmospheric conditions connected to the occurrence of extreme and oppressive heat events across the contiguous US. We use a variety of atmospheric variables

in our analysis at both the daily and monthly resolutions (Table S1 in the supporting information). Additionally, we augment ERA-Interim analysis with data sets from the North American Regional Reanalysis product (Mesinger et al., 2006). We compare the ERA-Interim findings with contemporaneous results from North American Regional Reanalysis to check for consistency between products and reflect on robustness of the results to the chosen data set.

Monthly soil moisture anomalies (0–40 cm) between June and August (1979–2016) are obtained from the Noah Land Surface Model as part of the North American Land Data Assimilation System, Phase II (Ek et al., 2011; Xia et al., 2012). Precipitation data for spring (March–May, MAM) and summer (June–August, JJA) are obtained from the Parameter Regression on Independent Slopes Model (Daly et al., 1997) monthly, 4-km horizontal resolution product. These data sets are used to assess the influence of surface-atmosphere hydrology on defining the U.S. heat wave characteristics during SIE extreme phases.

2.1.2. SIE and Melt Onset

We use monthly SIE records spanning March–August, 1979–2016, from the National Snow and Ice Data Center Sea Ice Index (Fetterer et al., 2017) for the 14 Arctic regional seas shown in Figure S1. To assess the timing of sea ice melt onset during low HB SIE summers, we utilize data compiled by Markus et al. (2009) updated to 2016. For each time series, the data are detrended using least squares linear regression to isolate the interannual variations in SIE; the standardized residuals are used to aggregate data into mean spring (MAM) and summer (JJA) conditions and to identify extreme years of SIE for each Arctic regional sea.

2.1.3. Teleconnection Indices

To assess the potential influence of various large-scale oceanic and atmospheric states on the observed linkages between Arctic SIE and summer U.S. heat waves, we study the association between SIE and various teleconnections known to influence ice melt and U.S. heat wave frequency. Time series of each index are examined for the 1979–2016 period. At the interannual time scales these include El Niño-Southern Oscillation (ENSO; November–August), the NAO, and the Greenland Blocking Index (GBI; both March–August). ENSO reflects the year-to-year variability of the ocean-atmosphere system in the equatorial Pacific. The Oceanic Niño Index is used to capture the state of ENSO and represents the 3-month running mean SST anomalies (Huang et al., 2017) in the Niño 3.4 region (5 °N–5 °S; 170 °W–120 °W). The NAO captures the covariation of atmospheric height fields between the Azores and Iceland through the leading empirical orthogonal function of monthly mean 1,000-hPa height anomalies poleward of 20° latitude (Barnston & Livezey, 1987). The GBI describes variations in the monthly mean 500-hPa geopotential height field over Greenland and bordering land-sea areas, 60–80 °N and 20–80 °W (Hanna et al., 2016). We also evaluate the influence of the annual index of the Pacific Decadal Oscillation and the Atlantic Multidecadal Oscillation (AMO) that capture the slow-varying state of SSTs over the Pacific and Atlantic basins, respectively.

2.2. Methods

Extreme and oppressive heat events are identified using the excess heat factor (EHF; Nairn et al., 2009). The EHF has been widely implemented to represent heat wave intensity and frequency in a variety of global regions (Perkins et al., 2012; Piticar et al., 2017; Rohini et al., 2016). EHF is a product of two separate heat wave metrics, the significance excess heat index (EHF_{sig}) and the acclimatization excess heat index (EHF_{accl}):

$$EHI_{sig} = \frac{T_{i-2} + T_{i-1} + T_i}{3} - T_{95} \tag{5}$$

$$EHF_{accl} = \frac{T_{i-2} + T_{i-1} + T_i}{3} - \frac{T_{i-32} + T_{i-31} + \ldots + T_{i-3}}{30}, \tag{6}$$

where T_i is daily T_{MAX} or T_E on day i, and T_{95} is the climatological 95th percentile of the T_{MAX} or T_E. The EHF_{sig} and EHF_{accl} are calculated over a 3-day window that moves 1 day at a time over the duration of the study period. The EHF is the product of the two metrics:

$$EHF = \max[1, EHI_{accl.}] \times EHF_{sig}, \tag{7}$$

where a positive EHF value represents a heat wave on day i. We compute daily EHF using T_{MAX} and T_E to represent extreme and oppressive heat events, respectively. Specifically, extreme heat is identified when the

T_{MAX}-based EHF is positive but the coincident T_E-based EHF value is not. Oppressive heat events are identified when both EHF values are positive.

Annual, summertime heat wave frequency is denoted as the number of events in which EHF is positive between 1 June and 31 August each year, 1979–2016. Frequencies are computed separately for extreme and oppressive heat waves, and annual summertime heat wave frequencies are then converted to anomalies by subtracting the overall 38-year (1979–2016) average frequency and dividing by the 38-year frequency standard deviation. Using frequency anomalies allows us to more efficiently determine outliers, as well as normalizing for statistical tests requiring standard distributions.

We use Pearson product-moment correlations to assess the relationship between summer conterminous U.S. heat wave frequencies and spring (−1 season lag) and summer (0 lag) SIE conditions across the various Arctic marginal seas. To further explore the connections between heat waves and extreme HB SIEs, we construct various composites depicting the average state of heat wave frequencies and that of various surface and atmospheric conditions during low SIE conditions. We begin by aggregating the 10 lowest and 10 highest summer SIE detrended anomalies into negative SIE (SIE−) and positive SIE (SIE+) years, with the remaining 18 years identified as SIE neutral (SIEn; Table S2). The mean composites associated with extreme SIE are subsequently differenced as follows to best isolate the extreme SIE signature in each surface-atmosphere variable: SIE− minus SIEn (of particular interest to this study and discussed most herein), SIE+ minus SIEn, and SIE− minus SIE+. The composite analyses and Pearson correlations are tested for statistical significance at the 95% and 99% confidence levels using a two-tailed *t* test.

3. Results

3.1. Marginal Ice Variability and Regional Expression of U.S. Summer Heat Waves

We compute the Pearson product-moment correlation coefficients between mean seasonal (MAM and JJA) SIE in each Arctic basin and mean regional JJA heat wave frequency (T_E and T_{MAX}) calculated across seven U.S. climate areas (Table S3 and Figure S2; Melillo et al., 2014). We also calculate the correlation coefficients between seasonal (MAM and JJA) SIE in each basin and heat wave frequency (EHF > 0) at each ERA-Interim grid cell (not shown). A careful review of the correlation results reveals that HB SIEs display the strongest relationship with both heat wave types (Figure S3). The strongest T_{MAX} heat wave frequency associations are located in the southern Plains (SP; Figure S3 top panel), and the strongest T_E heat wave relationships can be observed in portions of the Great Lakes and across the southeastern US (Figure S3 bottom panel). The region denoted as HB includes James Bay, Hudson Strait, and the Foxe Basin, where SIE variations are strongly influenced by atmospheric forcing (Wang et al., 1994). Sea ice melt begins across HB along its coastal regions in the northwest and northeast including James Bay in late May to early June; the southwestern coast of HB is the last to lose ice and the Bay is usually ice free by early August (Hochheim & Barber, 2014).

3.2. Summer U.S. Heat Waves and HB SIE Variability

We composite JJA extreme and oppressive heat wave frequency anomalies across the USA for extreme JJA HB SIE conditions (Figure 1) and differences between them (Figure S4) to further explore the nature of the relationships. Extreme and oppressive heat wave frequencies increase during SIE− years and decrease during SIE+ years across portions of the Midwest (MW), Northeast (NE), and the Southeast (SE) where the differences are most pronounced and statistically significant. A dipole pattern emerges in the frequencies of both extreme and oppressive heat waves (Figure 1) as the northwest US exhibits reduced (elevated) heat wave frequencies during SIE− (SIE+) years, generally opposite of the central and SE regions. The oppressive type is especially pronounced along the Gulf Coast.

We further quantify the heat wave day incidence variability as related to Hudson SIE by computing differences in mean summer frequency in each of the seven U.S. climate regions between SIE− and SIEn years and SIE+ and SIEn years (Table S5). Negative (low) SIE years on HB coincide with increases in extreme (T_{MAX}) heat wave days in the SP (14 days), MW (8 days), and SE (13 days) as compared with neutral SIE years. Increases in T_{MAX} heat wave days in these regions are significant at the 95% confidence level. Negative SIE anomalies are similarly associated with increases in oppressive (T_E) heat wave days in the SP (10 days), MW (8 days), and SE (11 days) as compared with neutral Hudson SIE years. Increased

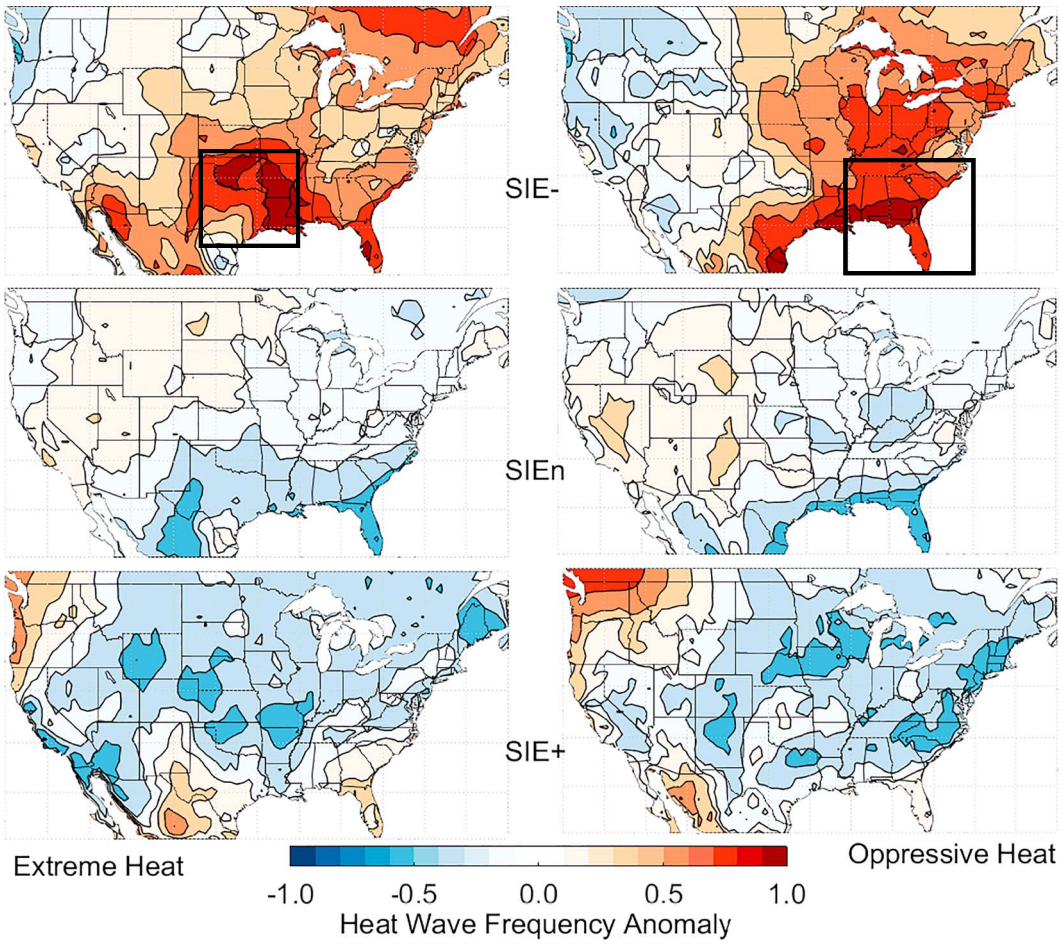

Figure 1. Composites of summer (left panel) extreme ($T_{\max}$) and (right panel) oppressive heat wave (T_E) frequency by Hudson SIE anomalies. Frequencies are expressed as standardized anomalies. Boundaries depicting the southern Plains (a) and the Southeast (b) regions, are shown using black boxes in the top panels. SIE = sea ice extent.

oppressive heat wave day incidence in the MW and SE is significant at the 99% confidence level and at the 95% confidence level for the SP.

The continental patterns of extreme and oppressive heat wave frequency anomalies are attributed to similar spatial variability in summertime average T_{MAX} and T_E (Figure 2). In particular, during low ice years (top panel), T_{MAX} increases (left panel) are maximized in the SP whereas T_E increases (right panel) are largest in a broader region spanning the mid-South to MW US. During SIE+ years there is a dramatic increase in T_E in the Pacific Northwest (bottom right panel); this region exhibits a nearly 2.5 °C increase in summer-averaged T_E between SIE+ and SIEn years. Given the robustness of results in the SP and across the SE we focus the remainder of our analyses on evaluating statistical connections between low summer HB SIEs and contemporaneous heat wave frequency observed in these regions.

Differences in the heat character (i.e., extreme vs. oppressive) experienced in the SP and large portions of the SE US during SIE− years are primarily attributable to contrasting anomalies of specific humidity (Figure S5a). The distinction of positive and negative near-surface specific humidity anomalies split along the 100th meridian reflects how near-surface humidity variations contribute to the oppressive heat events east of the 100th meridian, while below normal humidity levels coincide with the presence of extreme heat events west of the meridian. The south-central US is typically frequented by the Great Plains low-level jet during the summer, which is a fast-moving band of 900- to 800-hPa southerly winds that serve as important source of southerly moisture and warm air from the Gulf of Mexico across the SP (Higgins et al., 1997). However, the results presented here show positive specific humidity anomalies spanning 95 to 80 °W

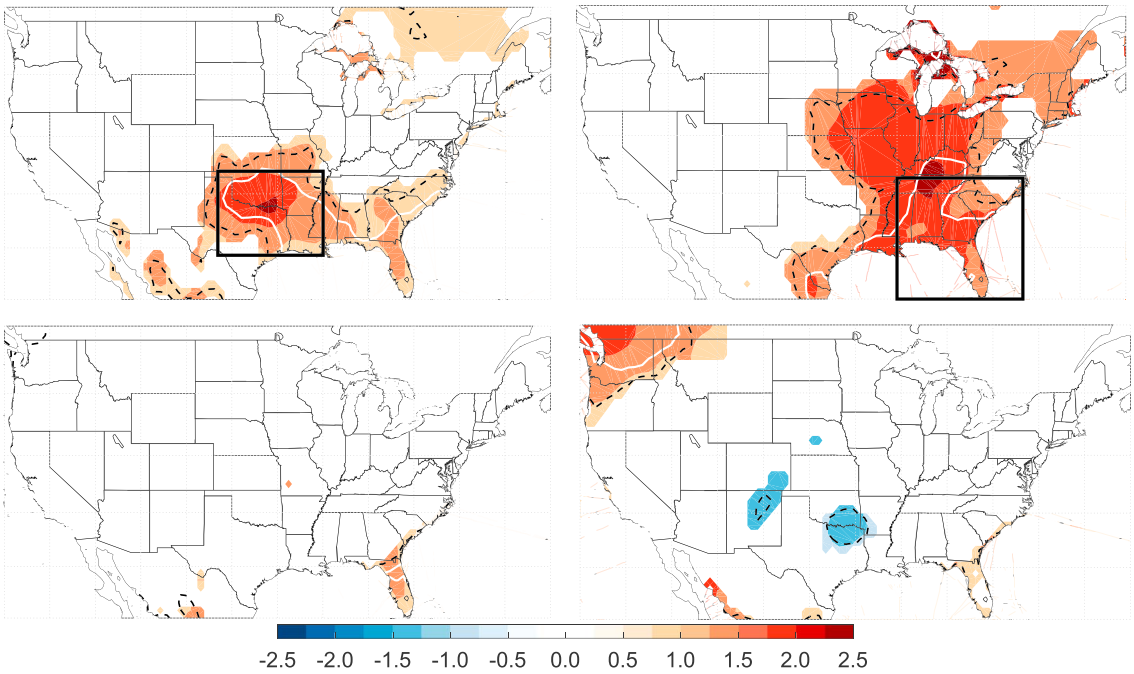

Figure 2. Difference maps of summer average (left panel) T_{max} and (right panel) T_E (°C). Maps show differences between (top panels) Hudson SIE− and SIEn years and (bottom panels) SIE+ and SIEn years. Black (white) contour lines denote significant correlations at the 95% (99%) confidence level.

longitude that are primarily located below 950 mb (Figure S5a). This suggests that the enhanced near-surface humidity does not correspond with a strengthened low-level jet; composites of concurrent meridional wind anomalies (Figure S5b) demonstrate the lack of low-level southerly flow over the entire central US during SIE− summers.

An alternative explanation for the enhanced humidity observed in large sections of the southeastern US and increased T_E in the mid-South and portions of the MW regions during low summer SIE− conditions is increased local moisture availability. Summer soil moisture anomalies (0–40 cm) show increased soil water availability throughout large portions of the eastern sections of the MW and the mid-South regions along with reduced soil water availability in the SP (Figure 3a). These spatial patterns of summer soil moisture anomalies are likely driven by similar patterns in antecedent (spring) and concurrent (summer) precipitation (Figures 3c and 3d). Enhanced spring and summer precipitation and corresponding increased soil moisture availability in large sections of the MW and mid-South regions coincide with decreases in both precipitation and soil moisture in the SP (Figure 3a). In particular, limited soil moisture availability during SIE− summers constrain evapotranspiration rates in the SP by as much as 0.5 mm per day (Figure 3b) considerably reducing the land surface contribution to near-surface atmospheric humidity.

3.3. Spring Surface and Synoptic Conditions

Interannual and long-term trends in summer SIE across HB have been shown to be influenced by large-scale atmospheric circulation variability and wind anomalies surrounding the region during the previous spring (Ogi et al., 2016; Qian et al., 2008). Qian et al. (2008) found a strong, positive correlation ($r = 0.67$, $p < 0.01$) between detrended spring near-surface air temperatures over HB and detrended HB SIE one season later. Sea ice melt and open water development enhance surface absorption of radiation that is subsequently released back to the atmosphere influencing early summer SIE conditions across the region. Tivy et al. (2011) show that at least 30% of the sea ice cover variation in the summer across HB and the Foxe Basin is linked to spring surface air temperatures and Hochheim and Barber (2014) argue that spring surface air temperatures determine up to 80% of SIE and break up date variation with the remaining influence due to wind forcing. Figure 4a confirms these studies and shows the mean conditions of the 1,000-hPa temperature anomalies during the 10 lowest JJA HB SIE years. The anomalously warm spring lower tropospheric conditions that reach over 2 °C (statistically significant at the 99% confidence level) over the HB and

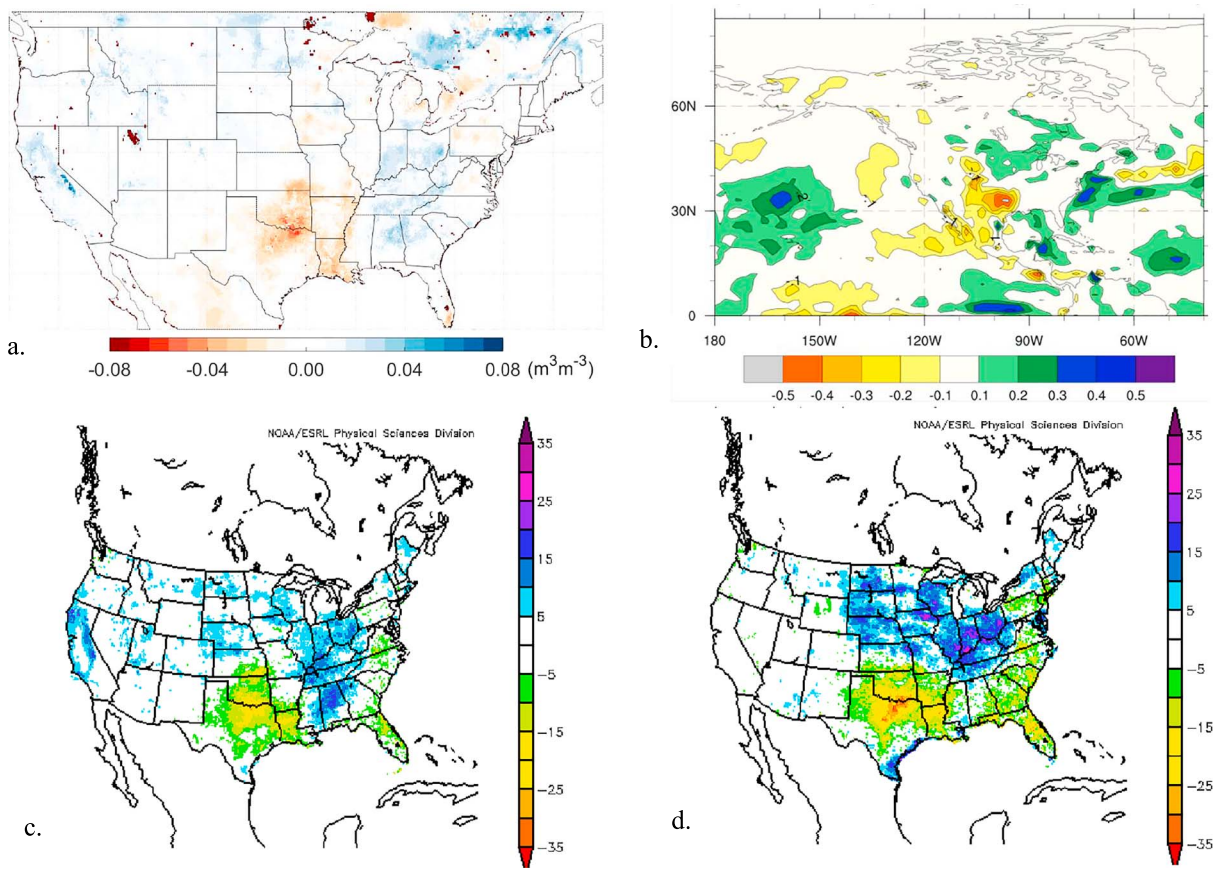

Figure 3. Panel (a) shows summer average (0–40 cm) soil moisture anomalies (m^3/m^3) during Hudson SIE− years. Panel (b) shows summer average evapotranspiration rate anomalies (mm/day) during Hudson SIE− years. Panels (c) and d show spring (c) and summer (d) total precipitation anomalies during Hudson SIE− years (mm).

Labrador areas are evident. Coincidental with the surface warming over land are SST anomalies exceeding +0.5 °C throughout much of the western north Atlantic including Labrador Sea, Baffin Bay, and southern portions of Greenland Sea (Figure 4b).

This expansive warming coincides with a simultaneous surface atmospheric ridge over the high latitudes of the NH (Figure 4c). This feature, also identified by Ogi et al. (2016), emanates from the Arctic basin toward Greenland and the western Atlantic basin. Statistically significant negative sea level pressure anomalies are present throughout the middle latitudes of the extratropical Atlantic basin. Vihma (2014) shows that low HB ice conditions tend to promote a stationary wave pattern that displaces the upper-level jet south, forcing storm tracks equatorward; the study also points toward a linkage between both Bering Sea ice extent and Hudson Bay extent that together contribute to the observed modifications in the atmospheric wave patterns across the Atlantic and Pacific. A composite analysis of sea level pressure anomalies for SIE− years in our study reveals an area of negative anomalies over the Bering Strait between winter and the following summer months (not shown). Correlation analyses performed in this study, however, did not confirm the Bering Sea connection in the spring; summer correlations could not be computed as the Bering Sea is ice free in August. The presence of a warm local atmosphere over HB has a preconditioning effect that results in unseasonably early sea ice melt onset (MO) in the region by 5.5 days preceding low SIE summer in the Bay (Table 1). Eight of the 10 low SIE years coincide with earlier than average melt typically occurring either 30 or 31 May; four of those dates fall below one standard deviation from the climatological mean. These conditions allow earlier open ocean absorption of heat energy, impacting the summer melt.

The atmospheric circulation/wind flow at sea level is mirrored in the middle (and upper—not shown) atmosphere and resembles the negative phase of the NAO/AO with its main centers of action displaced toward the west (Figure 4d). The positive geopotential height anomalies over the Arctic Basin extend south and

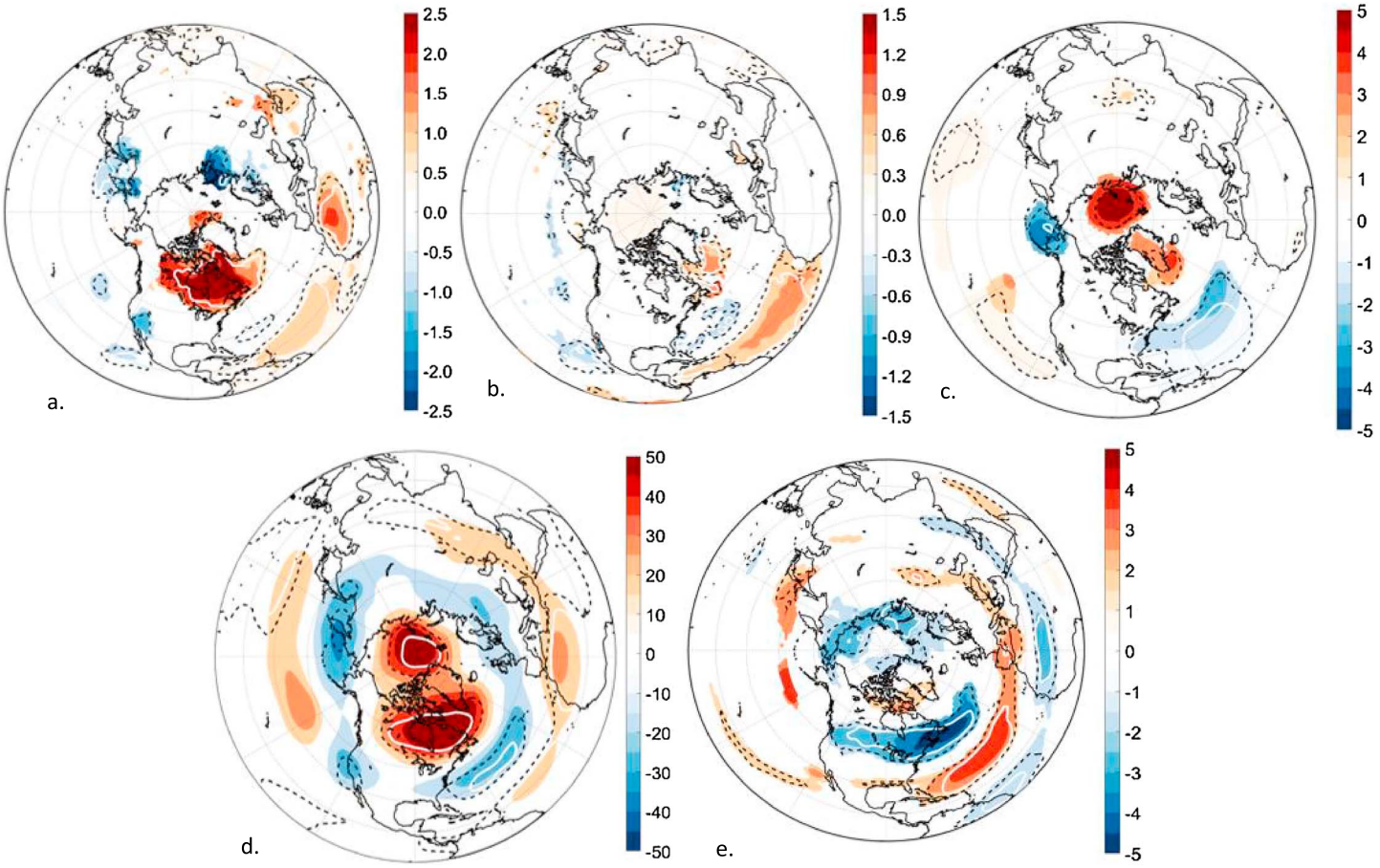

Figure 4. Mean spring (March–May) surface and synoptic conditions differences associated with low (SIE− minus SIEn) HB summers (June–August), 1979–2016. (a) 1,000-hPa temperature anomalies (°C), (b) SST anomalies (°C), (c) SLP anomalies (mb), (d) 500-hPa geopotential height anomalies (m), and (e) 500-hPa u-wind anomalies (m/s). Black (white) contour lines denote significant correlations at the 95% (99%) confidence level. Unless otherwise indicated ERA-Interim data was used to construct the captions.

east over Greenland, HB, and Labrador. The northern feature resembles the positive phase of the GBI typically associated with the negative phase of the NAO (Hanna et al., 2018). Anticyclone conditions emanating from these anticorrelated modes influence summer warming and melt over Greenland, Davis Strait, and HB (Hanna et al., 2014, 2016, 2018; Tedesco et al., 2016). Table 2 shows the spring NAO and GBI indices in the lowest 10 SIE summers in HB. Negative (positive) NAO (GBI) indices are observed in nine out of the 10 SIE− years; three (four) of the 10 lowest years reached values below (above) 1σ. The anomalous warming over much of Canada and the Arctic basin at this time appears to reduce the meridional temperature gradient weakening the zonal wind flow over the region (Figure 4e) by 2.5 °C at the 1,000-hPa level when compared to neutral sea ice years; a reduced gradient is present throughout the troposphere to the 300-hPa level (not shown).

3.4. Summer Surface and Synoptic Conditions

The most notable anomalies in atmospheric conditions observed during summer are in the 500-hPa geopotential heights over North America, near-surface/tropospheric air temperatures over the southern/central US, and the pattern of the jet flow over the NA continent (Figure 5). Summer synoptic flow anomalies in the midtroposphere and at the jet stream levels show the formation of an omega block centered over much of the eastern US and SP in June (Figure 5b) coupled with increased geopotential heights over the north Pacific south of the Aleutian Islands and Alaska. These modifications suggest the presence of ridge-trough-ridge pattern of atmospheric circulation and a stationary wave train. Such features have been documented as responses to declining sea ice in various areas of the Arctic including HB and Labrador Sea (Budikova et al., 2017; Vihma, 2014). The resultant atmospheric flow would bring consistent streams of

Table 1
Associations Between 10 Lowest HB SIE Summers, HWI, HB MO Days, and Various Teleconnections Known to Influence Summer Heat Waves in the Contiguous US

Year	HWI*	Hudson Bay MO day*	ENSO (JJA)	ENSO (Jan–Aug)	ENSO (Nov–Apr)	PDO	AMO	NAO JJA	NAO MAM	GBI MAM	GBI JJA
1979	−0.7	−4.3	0.1	0.1	0.1	−0.3	−0.9	1.9	−1.3	1.0	−1.0
1980	1.6	4.5	0.4	0.6	0.4	0.4	−0.1	−1.5	−0.5	0.3	0.7
1981	−0.1	−0.1	−0.6	−0.5	−0.2	0.7	−0.6	0.1	−0.6	0.1	−0.2
1998	2.1	−7.9	−1.2	1.2	1.7	0.9	1.6	−1.6	−0.8	0.7	1.2
1999	0.5	−15.1	−1.7	−1.9	−1.1	−1.3	1.2	0.4	−0.1	0.7	−0.8
2001	−0.2	−6.9	−0.1	−0.6	−0.6	−0.9	0.1	−0.1	−0.9	0.8	0.1
2005	1.4	−7.1	0.1	0.6	0.5	0.4	1.5	0.0	−2.0	1.7	0.2
2006	1.0	−10.3	0.2	−0.5	−0.5	−0.4	1.4	0.1	−0.9	1.1	0.2
2010	2.2	−9.7	−1.4	0.5	0.9	−0.3	1.5	−1.2	−1.9	2.1	1.6
2011	2.5	1.9	−0.6	−1.3	−1.0	−1.7	1.0	−2.1	1.3	−2.2	1.9
1981–2010 mean	0	150.9	0	0	0	0	0	0	0	0	0
1981–2010 stdev	1	8.1	1	1	1	1	1	1	1	1	1
# years > +1σ	6	0	0	1	1	0	6	1	1	4	3
# years < −1σ	0	4	3	2	2	2	0	4	3	1	1
# years > 0	7	2	4	5	5	4	7	5	1	9	7
# years < 0	3	8	6	5	5	6	3	5	9	1	3

Note. Values for all variables except for HWI* and HB MO** day anomalies are standardized. AMO = Atlantic Multidecadal Oscillation; ENSO = El Niño–Southern Oscillation; GBI = Greenland Blocking Index; Hudson Bay; HWI = Heat Wave Index; JJA = June–August; MAM = March–May; MO = melt onset; NAO = North Atlantic Oscillation; PDO = Pacific Decadal Oscillation; SIE = sea ice extent.

warm air from the desert southwest into the study area and increase the potential for heat waves to form throughout the summer season. The summer polar jet shows significant north-south meandering over the NH during low SIE summers in HB (Figure 5c).

The NA block initially forms between late May and early June and persists over the area through August (Figure 5d). Maximum ridging is located over the SP between the middle of June and into late July. Subsidence throughout most of the troposphere over the central US, as indicated by the presence of positive omega anomalies (Figure S6), is also suggestive of elevated middle- to upper-level tropospheric geopotential heights. The conditions are conducive to elevated surface/atmospheric air temperature and increased incidence of heat waves. The atmospheric blocking pattern situated over the southern US enhances southerly air flow into the Plains and eastern U.S. regions; positive surface temperature conditions first appear in June (not shown) and last throughout the summer (Figure 5f) with maximum warming in excess of 1 °C centered over the SP region. Statistically significant temperature anomaly magnitudes span an area from the SP into the SE. The conditions extend throughout the atmospheric column over this area with temperature anomalies >0.5 °C observed to the 150-hPa level.

3.5. Extreme Summer Heat Wave Conditions—Case Studies

To further explore the associations between HB sea ice conditions and U.S. heat wave characteristics, we examine the atmospheric conditions associated with specific heat wave summers when the frequencies have been among the highest/lowest during the studied time period. Regional summer heat wave frequencies are determined by computing the total number of heat wave days in each of the two U.S. regions best captured by the mean composite difference in summer frequency of heat waves associated with SIE− summers displayed in Figure S4. The frequency time series (T_{max} for SP and T_e for the SE) are then standardized and an overall standardized heat wave frequency index (HWI) is computed by adding the two regional frequencies and standardizing the resultant series. Seven of the 10 years with highest HWI coincide with one of the 10 lowest HB SIE summers (Table 1), and nine highest HWIs coincide with lower-than-expected SIE conditions (not shown). It is, therefore, not surprising that the atmospheric and surface conditions associated with some of the most extreme heat wave conditions across the study areas (not shown) closely resemble those shown in Figures 4 and 5. We examine in detail the surface and synoptic characteristics associated with

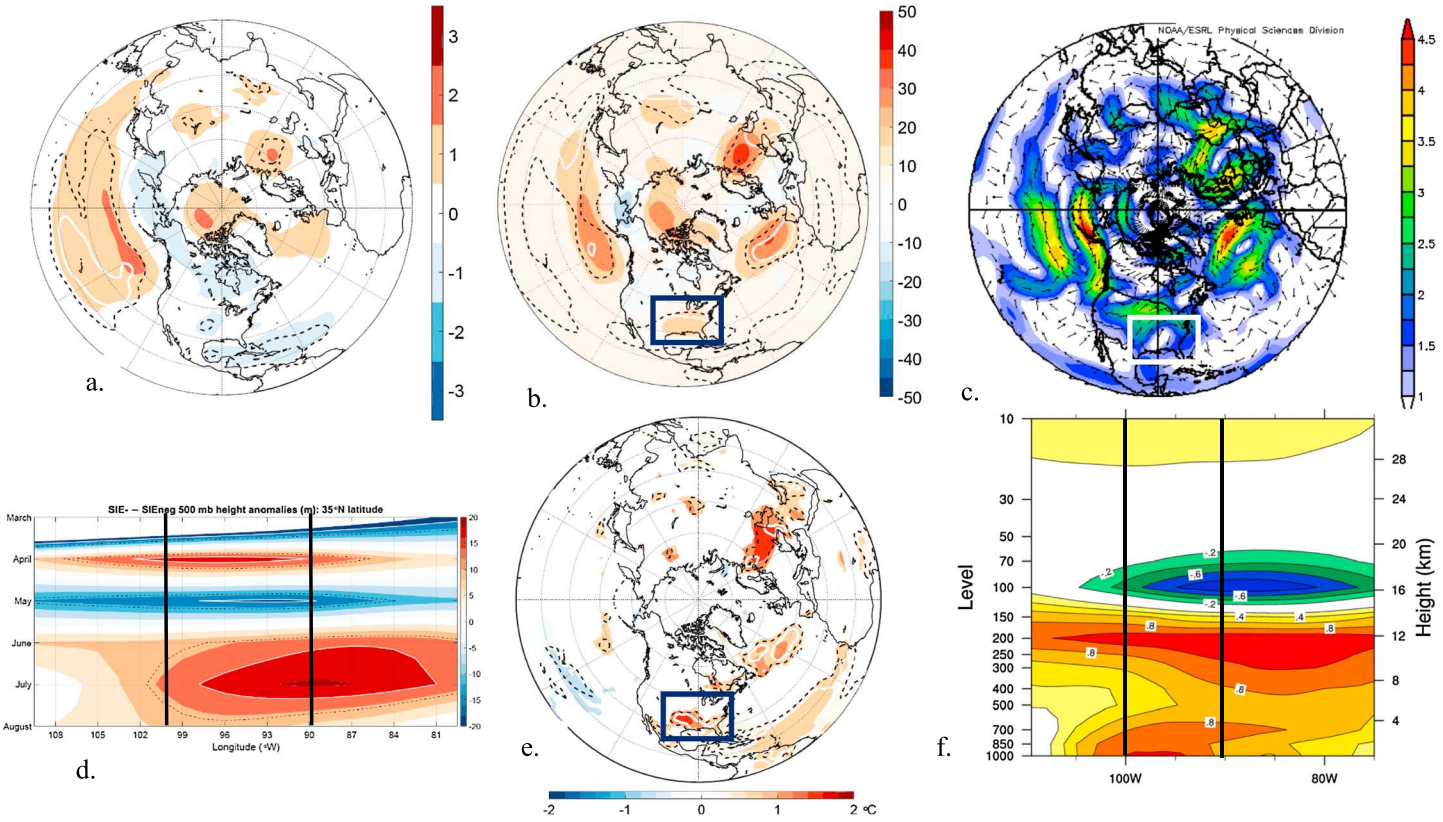

Figure 5. Mean summer (June–August) surface and synoptic conditions differences associated with low (SIE− minus SIEn) HB summers (June–August), 1979–2016. (a) SLP anomalies (mb), (b) 500-hPa geopotential height anomalies (m), (c) 250-hPa vector wind anomalies (m/s; NCEP/NCAR Reanalysis), (d) Hovmoller plot (March–August evolution) of 500-hPa geopotential height anomalies at 35 °N, 80–110 °W, (e) 1,000-hPa air temperature anomalies (C), and (f) longitude-altitude plot of air temperature anomalies (C) from 30 to 40 °N longitudinal boundaries span from 75 to 110 °W. Contour interval is 0.2 C. Black (white) contour lines in panels a–e denote significant correlations at the 95% (99%) confidence level. The approximate boundaries of our US study area are indicated in b–f. SE U.S. regions extends east of 90 °W and SP east of than 100 °W. Unless otherwise indicated ERA-Interim data was used to construct the captions.

two cases of extreme heat wave summers, 1998 and 1992 (Figures S7–S10). The 2 years represent contrasting SIE and HWI conditions, 1998 coinciding with third largest number of heat waves across the SP and SE regions when HB SIEs ranked among the 10 lowest; 1992 ranks the lowest in incidence of heat waves in these areas and among the 10 highest HB SIE levels.

The low SIE summer conditions in 1998 are preceded by an atmospheric and oceanic warming over the northern latitudes of the NH (anomalies exceed 1 °C over the Labrador/HB region) including the western North Atlantic basin (Figures S7a and S7b). These conditions coincide with a midtropospheric ridge over the high latitudes of the NH (Figure S7c); the spring NAO and GBI patters in 1998 were recorded at −0.8 and 0.7, respectively (Table 2). Patterns of surface pressure (Figure S7d) and associated near-surface winds (Figure S7e) in the spring show the advection of relatively warm air to the HB area from the west, likely contributing to the ~8 days earlier than average melt onset. The anomalous atmospheric warming in the higher latitudes reduces the meridional temperature gradient between the high and middle latitudes of the NA continent by about 2.5 °C at the 1,000-hPa level, and the reduced gradient is observed to the 300-hPa level (not shown). These conditions may reduce the midtropospheric zonal wind flow in spring over the eastern sections of the continent (Figure S7f). The atmospheric warming spreads toward the east and to the south in the summer with anomalously warm near-surface air temperatures covering much of the continent reaching anomalies over 2 °C over large portions of the southern US (Figure S8b). The warming extends throughout the troposphere to 150 hPa (Figure S8c). At this time, near-surface winds (Figure S8d) show an anomalous easterly to southeasterly flow. The synoptic flow over the continent is characterized by the presence of elevated geopotential heights over large regions of the north Pacific and the southern US/Mexico region (Figure S8a). High incidence of T_e and T_{max} heat waves in the SE and SP regions, respectively, is in part

shaped by the presence of anomalously high and low specific humidity levels in the atmosphere evident over the two regions (Figure S8e). The surface and atmospheric conditions between spring and summer observed in 1998 closely resemble those presented by the overall composites constructed for the 10 lowest HB SIE summers shown in Figures 4 and 5.

Spring and summer conditions in summer 1992 show significant differences to those observed in 1998. Anomalously cool spring conditions (Figure S9a) with unseasonal near-surface northerly airflow over Labrador and Baffin Bay and into HB (Figure S9e) likely kept SIE above normal in the region throughout the spring and into the summer. The ice melt onset day at HB occurred on day 165 that year which is almost 14 days (1.7σ) later than the 1979–2016 average. The north Atlantic Ocean was relatively cool that spring also especially along the Labrador coast and south of Baffin Bay and Greenland (Figure S9b). Surface and midtropospheric circulation anomalies over the Atlantic resemble NAO+ and GBI- (Figures S9c and S9d) with anomalously low midtropospheric geopotential heights covering large regions of the Arctic and the middle latitudes of the Pacific with a trough positioned over the eastern portions of NA. These conditions would promote northerly airflow into the lower latitudes of the continent from the north allowing the polar jet to migrate deep into the south (not shown). The summer was also cool throughout much of NA east of the Rocky Mountain range in the summer (Figures S10b and S10c) with the eastern sections of NA dominated by a well-developed midtropospheric trough that brought the a cold air from the north into the southern latitudes of the USA (Figure S10a) significantly reducing the potential of heat wave formation across the southern US.

3.6. Teleconnective Influences

In addition to the aforementioned influences of the NAO and GBI, we also consider the influence of other atmospheric teleconnective features known to shape the background state of atmospheric variability and potentially modify the relationship between U.S. heat waves and sea ice decline in the HB region. Ding et al. (2014) and Chylek et al. (2009), respectively, point to the linkage between recent Arctic warming across northeastern Canada and Greenland and the state of the equatorial Pacific (i.e., ENSO) at interannual timescales and the state of the Atlantic Ocean thermohaline circulation or AMO at multidecadal timescales. Liu et al. (2004) document the interannual influence of the ENSO and AO on eastern Arctic sea ice including HB. Table 1 presents the indices of the teleconnection patterns known to influence climate including air temperature across eastern US in summer, namely, those associated with ENSO, Pacific Decadal Oscillation, AMO, NAO, and GBI during low-HB sea ice summers; indices of consequence here are highlighted in gray. Low ice summers do not show any particular preference for either phase of the ENSO outside of summer and back to the previous fall. We note, however, that six of the 10 SIE− years coincide with La Niña conditions in the equatorial Pacific during the summer months, results that are consistent with Wang et al. (1994) and Liu et al. (2004) who find by analyzing data for all months of the year that low sea ice conditions in HB coincide with simultaneously occurring negative NAO and La Niña conditions in the equatorial Pacific. NAO and GBI show the greatest association to low-ice conditions in HB in spring, with nine of the 10 years coinciding with negative phase of the NAO and positive phase of the GBI; only GBI retains influence into the summer months, however, in 7 years out of 10. Similar to Wang et al. (1994), we find no preference to either phase of the NAO during low ice summers in HB. The potential influence of the slowly varying north Atlantic SSTs as expressed by the AMO, however, is notable showing seven of the 10 lowest ice years (SIE−) occurring during positive phase of the AMO synchronous with anomalously warm extratropical Atlantic basin SSTs. Also, evident is a high coincidence of warm north Atlantic Ocean (AMO+) conditions with enhanced incidence of blocking, or GBI+ (9/10 years) over the Greenland/West North Atlantic region (Table 1). The latter results are similar to those described for the winter season by Hakkinen et al. (2011). Further exploration is warranted as the background state of the Atlantic basin may pose influence on the potential atmospheric responses to declining HB sea ice conditions and concurrent incidence of heat waves in the USA.

Considering all 38 years between 1979 and 2016, 21 are AMO+ years and 11 coincided with lower-than-expected SIE in HB (SIE-Neu or SIE−) and 10 years coincided with higher-than-expected SIE (SIE+Neu or SIE+) conditions. Three of the 10 highest SIE summers, 2016, 2004, and 2013, coincided with some of the strongest AMO+ conditions. There is nearly an equal split between SIC+ and SIE− summers during AMO+ years. Similar probabilities are observed with respect to heat wave occurrence, where of the 21

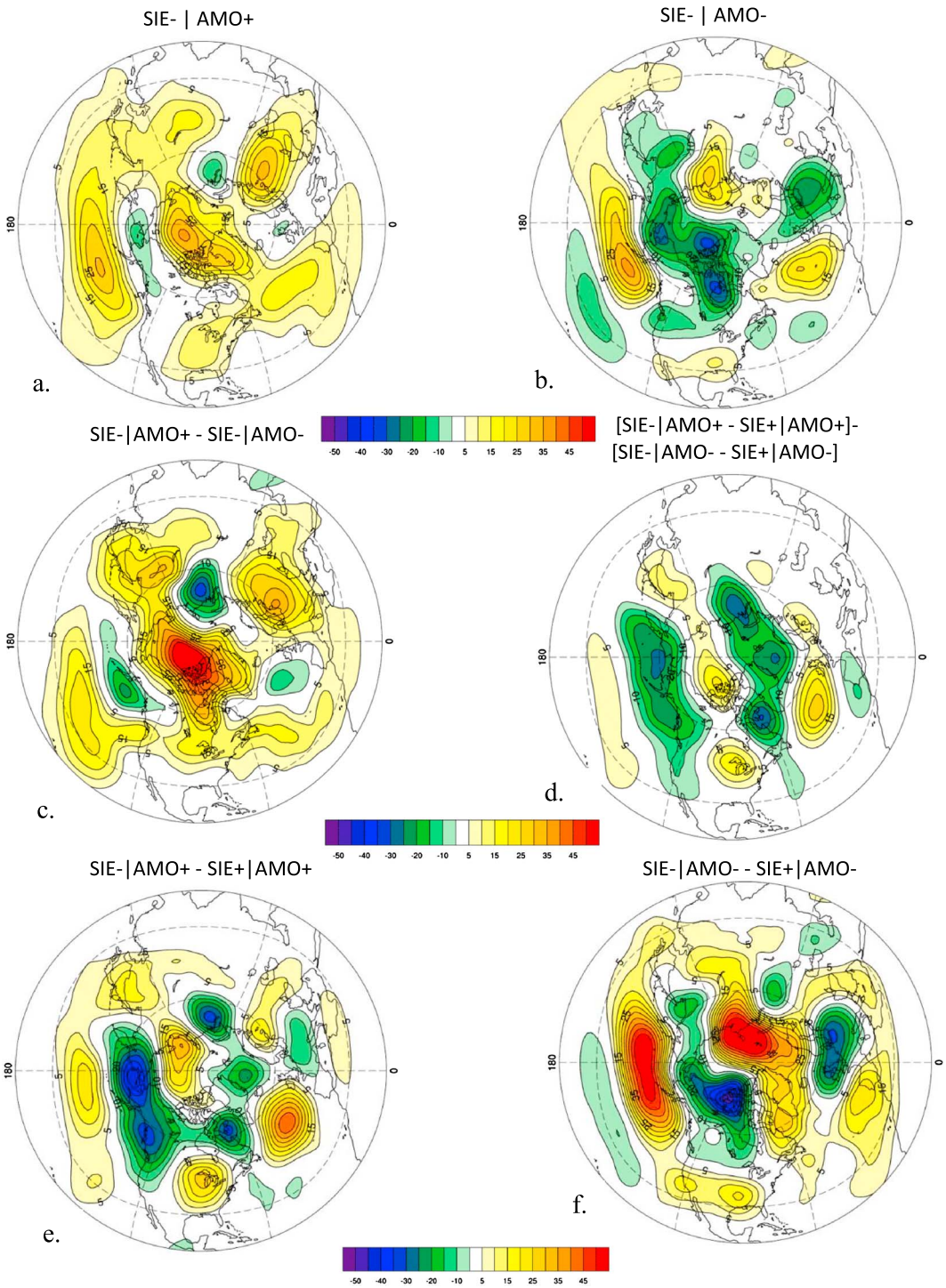

Figure 6. Mean June–August anomalies in the 500-hPa geopotential height (m) surfaces associated with extreme low (SIE−) HB sea ice conditions during (a) AMO+, (b) AMO−, and (c) their difference; (d) response to sea ice loss modulated by the AMO; (e) response to sea ice loss during AMO+ and; (f) response to sea ice loss during AMO−. Unless otherwise indicated ERA-Interim data was used to construct the captions. AMO = Atlantic Multidecadal Oscillation; SIE = sea ice extent.

AMO+ summers, 12 (57%) coincided with higher-than-expected southern U.S. heat wave frequencies. Together, these probabilities suggest that it is unlikely that the AMO is solely responsible for the decline in HB SIE and increase of heat wave frequencies in the southern US during summer. It is, however,

plausible that the slow-varying background state of the Atlantic basin as described by the positive state of the AMO in recent decades and in our study may act to modulate the atmospheric response of sea ice decline and modify the SIE/heat wave relationships.

Using a compositing approach similar to Osborne et al. (2017), we attempt to explore the potential influence of the AMO on the SIE/heat wave relationships by examining 500-hPa geopotential height anomalies. We classify the 20 extreme SIE years by the phase of the AMO as specified by the January–August AMO index into four AMO|SIE combinations (Table S4) and construct mean composite maps for each pair. We note the extremely limited number of degrees of freedom in this analysis. First, we assess the influence of the AMO during low SIE years only. The results shown in Figures 6a–6c indicate an expected increase in geopotential heights throughout large portions of the NH with notable elevations of the 500-hPa geopotential height level observed over an area spanning from the central Arctic toward Greenland and HB during AMO+ years; these conditions are coupled with reduced heights in the north Pacific south of Alaska (Figure 6c). The AMO influence is lacking over the southern and SE sections of the USA, our study area, in these results. Next, we quantify the summer atmospheric "response" to sea ice loss in HB during AMO+ and AMO− separately, by constructing mean difference composite maps (e.g., [SIE−|AMO+ minus SIE+|AMO+], for AMO + and [SIE−|AMO− minus SIE+|AMO−], for AMO−; Figures 6e and 6f). We note the presence of an anomalous midtroposheric ridge situated over our study area during both AMO+ and AMO− years. During the former the ridge resides over a large area encompassing the eastern US/southern Canada; during the latter, its influence is dominant over the southern portions of the USA, from coast to coast. The two zones of ridging encompass our U.S. study area.

The overall AMO modulation of the atmospheric response to sea ice loss is assessed here by examining the differences between the two above responses (Figure 6d). Its atmospheric influence over the eastern US is again most notable in the Midwestern/Great Lakes region through locally increased geopotential heights and near-surface air temperatures (not shown), owing to the eastern US ridge that is elongated toward the north during AMO+ years. The influence of AMO+ is also again evident over the high latitudes of the north Pacific around Alaska and along the Pacific coast where geopotential heights decline (Figure 6d). A comparison of this pattern of influence to that noted in Figure 5b suggests that AMO+ may act to increase the meandering of the jet flow over the NA continent that moves deeper to the south in the west and farther north in the east, amplifying the atmospheric wave train, during summers when sea ice levels are low in HB. Using a modeling approach, Osborne et al. (2017) found the winter atmospheric response to sea ice decline across the PNA region to be sensitive to the state of the AMO, with a high-low-high wave train depicting atmospheric flow from the north Pacific through the NA continent, during AMO− phase. Together, these results provide supporting evidence to the hypothesis that decline in HB SIE may play a notable role in shaping the ensuing atmospheric response over North America, especially in its eastern sector, including the central and SE US. The changes act to increase atmospheric temperatures and incidence of summer heat waves in the U.S. area.

4. Discussion and Conclusions

Using statistical analyses involving a multitude of surface and atmospheric conditions (i.e., anomalies in surface moisture, evapotranspiration, precipitation, surface and atmospheric air temperature, sea level pressure, middle- and upper-level geopotential heights and winds, and SST), this study examines the relationships between U.S. summer heat wave frequencies and regional spring and summer Arctic sea ice conditions. Our results reveal a series of boundary and atmospheric circulation patterns suggestive of a potential influence of summer HB sea ice conditions on same season heat wave frequency across the SP and SE regions of the USA. The interaction of the various conditions appears to be initiated one season ahead in spring with anomalous surface (land and ocean) and atmospheric warming across portions of northeastern Canada, including HB, the Arctic, and large sections of the northwestern Atlantic and Greenland. This warming is facilitated by near-surface winds (reinforced by a collocated atmospheric ridge) that advect warm air into the HB region. Such conditions coincide with earlier than normal sea ice melt and surface heat absorption in the HB region. The anomalous heating likely influences the formation of a persistent thermal ridge that coincides with slower zonal (westerly) winds, potentially as a result of reduced poleward thermal gradient observed between HB and eastern US/Canada in spring. These results are consistent with Arctic-midlatitude "linkage" studies as detailed by Vihma (2014) and Cohen et al. (2018). Coumou et al. (2015)

suggest that a reduction of the north-south thermal gradient and mean zonal winds may act to lessen the total atmospheric eddy kinetic energy and increase the amplification of quasistationary waves throughout the NH. Our results indicate the presence of atmospheric blocking that persists throughout the summer months over eastern NA. Associated with this block is increased summertime warming throughout the atmospheric column with maximum surface heating >1.5 °C collocated with the ridge over the SP.

The observed response of atmospheric flow over NA during low Hudson SIE summers is consistent with previous studies (Budikova & Chechi, 2016; Tang et al., 2013) and suggests greater meridional flow across the continent with increased incidence of troughing and ridging in the western and eastern US, respectively. The Greenland blocking pattern, observed here in spring and summer, has been recognized to enhance meridionality in the hemispheric atmospheric circulation as well, in part, through the displacement of the jet southward (Hanna et al., 2018). This pattern prompts southeasterly transport of warm, moist air into Baffin and HB that further influences the regional melt and local warming (Ballinger et al., 2018; Hanna et al., 2014, 2016, 2018).

During the 1979–2016 period, low sea ice summers in HB have coincided with higher frequency of extreme (i.e., low humidity) heat waves in the SP and oppressive (i.e., high humidity) heat waves across large portions of SE and portions of MW US. The distinct heat wave character can be accounted for by local surface and atmospheric conditions during the preceding spring and during the summer months. Both areas are overlain with a large-scale atmospheric blocking that advects southerly air and heat into the regions, with maximum atmospheric heating observed over the SP. The heat waves in the SP are preceded by anomalously dry spring conditions with low surface moisture and atmospheric humidity; dry conditions continue into the summer in this area. Large portions of the SE are wetter than normal in the spring with adequate-to-surplus soil moisture conditions and increased atmospheric humidity in the summer. Precursor surface and atmospheric moisture (mainly in the spring) appears to ultimately shape the nature of the heat waves associated with low summer sea ice conditions in the HB.

The series of proposed atmospheric modifications includes important interactions between modes of natural climate variability and the state of low-frequency SSTs over the north Atlantic basin and along eastern NA. Our results suggest that antecedent (i.e., spring) warm north Atlantic land-ocean surface temperatures along with strong atmospheric ridging over the northwestern Atlantic and eastern Canada resembling the negative (positive) NAO (GBI) appear to characterize the large-scale, spring ocean-atmosphere state linking summer SIE in HB and U.S. heat waves (Overland, 2016; Overland et al., 2016). These conditions have the potential to enhance early spring melt in the Bay that may in turn favor the development of unique summer surface and atmospheric conditions over the USA conducive to the formation of heat waves. Ballinger et al. (2018) identify a linkage between persistent and strong high pressure blocking and extreme early melt years of sea ice west of Greenland. We argue that the early onset of sea ice melt in HB in the spring may similarly enhance the strength of the surface and atmospheric warming and in turn further strengthen the blocking pattern over northeastern Canada throughout the season. These conditions in turn may support the development of the high-amplitude Rossby wave flow and atmospheric blocking systems in the middle latitude of the NH including the southern US in the following summer, paving the path to increased incidence of summer heat waves across the region.

This study offers a detailed analysis of observational records depicting various spring and summer surface, atmospheric, and oceanic conditions associated with reduced sea ice conditions across HB between 1979 and 2016. The purpose is to assess the viability of observed relationships between sea ice levels and the incidence of summer heat waves across the SP and SE regions of the USA as a first step in helping to gather evidence to establish a physical mechanism describing the connection between the two and further build on our existing knowledge of Arctic-middle latitude climate connections and influences.

Observational data sets are limited in length, here to only 38 years, posing a challenge when attempting to identify a signal in a highly variable atmosphere (e.g., AMO, SIE, and atmosphere interaction assessment). The difficulty in isolating the linkage mechanism using statistical methods alone is further compounded by the superimposed influence of various oceanic and atmospheric conditions that are known to shape either sea ice and/or extreme temperatures and potentially U.S. heat wave occurrence. Our results identify the role of one low-frequency variability in the Atlantic basin, particularly the AMO+ state, as one such influence that cannot be overlooked as it is known to impact extreme summer temperatures across eastern US

(Arguez et al., 2009) and has been dominating the slow-varying state of the Atlantic ocean-atmosphere system since the early 1990s. Recent literature on Arctic-middle latitude linkages recognizes that the mean background state of the ocean-atmosphere system may help shape the response of the atmosphere to sea ice variability in nonrandom ways, offering a potential to improve the predictions of the impacts resulting from sea ice decline at decadal timescales (Cohen et al., 2018; Osborne et al., 2017). Osborne et al. (2017) in turn argue that a particular state of the ocean-atmosphere system should be viewed as an advantageous phase for interpreting Arctic linkages with lower latitudes. Our results strive to build upon this work by providing observational evidence that speak to the potential influence of the positive phase of the AMO on the character of the atmospheric response to sea ice decline in HB.

Finally, it is important to point out that statistical analyses of observational records assessed here cannot rule out the influence of internal climate variability that may persist over seasonal timescales and act to simultaneously modify both SIE in Hudson Bay and southern U.S. heat wave frequency. Therefore, a necessary step forward in the process of determining the physical linkages responsible for these relationships will require the use of dynamical modeling methods that will allow for the relationships between sea ice variability and heat waves/atmospheric responses to be studied in isolation without the influence of random atmospheric fluctuations.

Acknowledgments
Data for the ONI index and the NAO index were downloaded from the CPC (http://www.cpc.ncep.noaa.gov/products/analysis_monitoring/ensostuff/ensoyears2011.shtml and http://www.cpc.noaa.gov/products/precip/CWlink/pna/nao.shtml). The PDO index was downloaded from the University of Washington (http://research.jisao.washington.edu/pdo/PDO.latest.txt), and the AMO index was downloaded from NOAA ESRL (https://www.esrl.noaa.gov/psd/data/timeseries/AMO/). The authors would like to thank Edward Hanna, University of Lincoln, UK, for sharing his GBI data and Jeffrey Miller, KBRWyle, Inc and NASA GSFC, for supplying the marginal melt onset dates. Many of the figures used presented were generated through the NOAA/ESRL Physical Sciences Division, Boulder, Colorado, from their website (https://www.esrl.noaa.gov/psd/). Other data sources are discussed in the Data section of the main manuscript and listed in the reference list.

References

Anderson, B. G., & Bell, M. L. (2009). How heat, cold, and heat waves affect mortality in the United States. *Epidemiology*, *20*(2), 205–213. https://doi.org/10.1097/EDE.0b013e318190ee08

Arguez, A., O'Brien, J. J., & Smith, S. R. (2009). Air temperature impacts over Eastern North America and Europe associated with low-frequency North Atlantic SST variability. *International Journal of Climatology*, *29*(1), 1–10. https://doi.org/10.1002/joc.1700

Ballinger, T. J., Hanna, E., Hall, R. J., Cropper, T. E., Miller, J., Ribergaard, M. H., et al. (2018). Anomalous blocking over Greenland preceded the 2013 extreme early melt of local sea ice. *Annals of Glaciology*, *59*, 181–190. https://doi.org/10.1017/aog.2017.30

Ballinger, T. J., & Sheridan, S. C. (2015). Regional atmospheric patterns and the delayed sea-ice freeze-up in the western Arctic. *Climatic Change*, *131*(2), 229–243. https://doi.org/10.1007/s10584-015-1383-5

Barnston, A. G., & Livezey, R. E. (1987). Classification, Seasonality and Persistence of low-Frequency Atmospheric Circulation Patterns. *Monthly Weather Review*, *115*, 1083–1126. http://doi.org/10.1175/1520-0493(1987)115<1083:CSAPOL>2.0.CO;2

Bentley, M. L., & Stallins, J. A. (2008). Synoptic evolution of Midwestern US extreme dew point events. *International Journal of Climatology*, *28*(9), 1213–1225. https://doi.org/10.1002/joc.1626

Bolton, D. (1980). The computation of equivalent potential temperature. *Monthly Weather Review*, *108*(7), 1046–1053. https://doi.org/10.1175/1520-0493(1980)108<1046:TCOEPT>2.0.CO;2

Budikova, D., & Chechi, L. (2016). Arctic sea ice and warm season North American extreme surface temperatures. *Climate Research*, *67*(1), 15–29. https://doi.org/10.3354/cr01349

Budikova, D., Ford, T. W., & Ballinger, T. J. (2017). Connections between north-central United States summer hydroclimatology and Arctic sea ice variability. *International Journal of Climatology*, *37*(12), 4434–4450. https://doi.org/10.1002/joc.5097

Chylek, P., Folland, C. K., Lesins, G., Dubey, M. K., & Wang, M. (2009). Arctic temperature change amplification and the Atlantic Multidecadal Oscillation. *Geophysical Research Letters*, *36*, L14801. https://doi.org/10.1029/2009GL038777

Cohen, J., Screen, J. A., Furtado, J. C., Barlow, M., Whittleston, D., Coumou, D., et al. (2014). Recent Arctic amplification and extreme mid-latitude weather. *Nature Geoscience*, *7*(9), 627–637. https://doi.org/10.1038/ngeo2234

Cohen, J., Zhang, X., Francis, J., Jung, T., Kwok, R., Overland, J., et al. (2018). In K. Uhlenbrock (Ed.), *Arctic change and possible influence on mid-latitude climate and weather. US CLIVAR Report 2018-1*, (p. 41). Washington, D.C. (USA): US CLIVAR. https://doi.org/10.5065/D6TH8KGW

Coumou, D., Kornhuber, K., Lehmann, J., & Petoukhov, V. (2017). Weakened flow, persistent circulation, and prolonged weather extremes in boreal summer. In S.-Y. Wang, J.-H. Yoon, C. C. Funk, & R. R. Gilles (Eds.), *Climate Extremes: Patterns and Mechanisms*, *Geophys. Monogr.* (Vol. 226, pp. 61–74, ISBN). Washington, D. C: American Geophysical Union. ISBN: 978119067849.

Coumou, D., Lehmann, J., & Beckmann, J. (2015). The weakening summer circulation in the Northern Hemisphere mid-latitudes. *Science*, *348*(6232), 324–327. https://doi.org/10.1126/science.1261768

Coumou, D., Petoukhov, V., Rahmstorf, S., Petri, S., & Schellnhuber, H. J. (2014). Quasi-resonant circulation regimes and hemispheric synchronization of extreme weather in boreal summer. *Proceedings of the National Academy of Sciences of the United States of America*, *111*(12), 331–12,336.

Daly, C., G.H. Taylor, & W.P. Gibson (1997). The PRISM approach to mapping precipitation and temperature. In Proc., 10th AMS Conf. on Applied Climatology, 20-23.

Davis, R. E., Hondula, D. M., & Patel, A. P. (2016). Temperature observation time and type influence estimates of heat-related mortality in seven US cities. *Environmental Health Perspectives*, *124*(6), 795–804. https://doi.org/10.1289/ehp.1509946

Dee, D. P., Uppala, S. M., Simmons, A. J., Berrisford, P., Poli, P., Kobayashi, S., et al. (2011). The ERA-Interim reanalysis: Configuration and performance of the data assimilation system. *Quarterly Journal of the Royal Meteorological Society*, *137*(656), 553–597. https://doi.org/10.1002/qj.828

Della-Marta, P. M., Haylock, M. R., Luterbacher, J., & Wanner, H. (2007). Doubled length of western European summer heat waves since 1880. *Journal of Geophysical Research*, *112*, D15103. https://doi.org/10.1029/2007JD008510

Diffenbaugh, N. S., & Ashfaq, M. (2010). Intensification of hot extremes in the United States. *Geophysical Research Letters*, *37*, L15701. https://doi.org/10.1029/2010GL043888

Diffenbaugh, N. S., Pal, J. S., Giorgi, F., & Gao, X. (2007). Heat stress intensification in the Mediterranean climate change hotspot. *Geophysical Research Letters*, *34*, L11706. https://doi.org/10.1029/2007GL030000

Ding, Q., Schweiger, A., L'Heureux, M., Battisti, D. S., Po-Chedley, S., Johnson, N. C., et al. (2017). Influence of high-latitude atmospheric circulation changes on summertime Arctic sea ice. *Nature Climate Change*, *7*(4), 289–295. https://doi.org/10.1038/nclimate3241

Ding, Q., Wallace, J. M., Battisti, D. S., Steig, E. J., Gallant, A. J. E., Kim, H.-J., & Geng, L. (2014). Tropical forcing of the recent rapid Arctic warming in northeastern Canada and Greenland. *Nature*, *509*(7499), 209–212. https://doi.org/10.1038/nature13260

Ek, M. B., Xia, Y., Wood, E., Sheffield, J., Luo, L., Lettenmaier, D., et al. (2011). North American Land Data Assimilation System Phase 2 (NLDAS-2): Development and applications. *GEWEX News*, *2*, 6–8.

Fall, S., Diffenbaugh, N. S., Niyogi, D., Pielke, R. A., & Rochon, G. (2010). Temperature and equivalent temperature over the United States (1979–2005). *International Journal of Climatology*, *30*(13), 2045–2054. https://doi.org/10.1002/joc.2094

Fetterer, F., Knowles, K., Meier, W., Savoie, M., & Windnagel, A. K. (2017). *Sea ice Index*, Version 3. Boulder, Colorado USA: NSIDC: National Snow and Ice Data Center, Sea ice index regional monthly data G02135 v2.1. https://doi.org/10.7265/N5K072F8 Accessed on October 31, 2017

Ford, T. W., & Schoof, J. T. (2017). Characterizing extreme and oppressive heat waves in Illinois. *Journal of Geophysical Research: Atmospheres*, *122*, 682–698. https://doi.org/10.1002/2016JD025721

Francis, J., & Vavrus, S. J. (2012). Evidence linking Arctic amplification to extreme weather in mid-latitudes. *Geophysical Research Letters*, *39*, L06801. https://doi.org/10.1029/2012GL051000

Francis, J. A. (2017). Why are Arctic linkages to extreme weather still up in the air? *Bulletin of the American Meteorological Society*, *98*(12), 2551–2557. https://doi.org/10.1175/BAMS-D-17-0006.1

Francis, J. A., & Vavrus, S. J. (2015). Evidence for a waiver jet stream in response to rapid Arctic warming. *Environmental Research Letters*, *10*(1). https://doi.org/10.1088/1748-9326

Francis, J. A., Vavrus, S. J., & Cohen, J. (2017). Amplified Arctic warming and mid-latitude weather: New perspectives on emerging connections. *WIREs Climate Change*, *8*(5). https://doi.org/10.1002/wcc.474

Hakkinen, S., Rhines, P. B., & Worthen, D. L. (2011). Atmospheric blocking and Atlantic multidecadal ocean variability. *Science*, *334*(6056), 655–659. https://doi.org/10.1126/science.1205683

Hanna, E., Cropper, T. E., Hall, R. J., & Cappelen, J. (2016). Greenland Blocking Index 1851–2015: A regional climate change signal. *International Journal of Climatology*, *36*(15), 4847–4861. https://doi.org/10.1002/joc.4673

Hanna, E., Fettweis, X., Mernild, S. H., Cappelen, J., Ribergaard, M. H., Schuman, C. A., et al. (2014). Atmospheric and oceanic climate forcing of the exceptional Greenland ice sheet surface melt in summer 2012. *International Journal of Climatology*, *34*(4), 1022–1037. https://doi.org/10.1002/joc.3743

Hanna, E., Hall, R. J., Ropper, T. E., Ballinger, T. J., Wake, L., Mote, T., & Cappelen, J. (2018). Greenland blocking index daily series 1851–2015: Analysis of changes in extremes and links with North Atlantic and UK climate variability and change. *International Journal of Climatology*, *38*(9), 3546–3564. https://doi.org/10.1002/joc.5516

Higgins, R. W., Yao, Y., Yarosh, E. S., Janowiak, J. E., & Mo, K. C. (1997). Influence of the Great Plains Low-Level Jet on summertime precipitation and moisture transport over the central United States. *Journal of Climate*, *10*(3), 481–507. https://doi.org/10.1175/1520-0442

Hochheim, K. P., & Barber, D. G. (2014). An update on the ice climatology of the Hudson Bay system. *Arctic, Antarctic, and Alpine Research*, *46*(1), 66–83. https://doi.org/10.1657/1938-4246-46.1.66

Huang, B., Thorne, P. W., Banzon, V. F., Boyer, T., Chepurin, G., Lawrimore, J. H., et al. (2017). Extended reconstructed sea surface temperature version 5 (ERSSTv5): Upgrades, Validations, and Intercomparisons. *Journal of Climate*, *30*(20), 8179–8205. https://doi.org/10.1175/JCLI-D-16-0836.1

Koenigk, T., Caian, M., Nikulin, G., & Schimanke, S. (2016). Regional Arctic sea ice variations as predictor for winter climate conditions. *Climate Dynamics*, *46*(1-2), 317–337. https://doi.org/10.1007/s00382-015-2586-1

Kunkel, K. E., Changnon, S. A., Reinke, B. C., & Arritt, R. W. (1996). The July 1995 heat wave in the Midwest: A climatic perspective and critical weather factors. *Bulletin of the American Meteorological Society*, *77*(7), 1507–1518. https://doi.org/10.1175/1520-0477

Liu, J., Curry, J. A., & Hu, Y. (2004). Recent Arctic sea ice variability: Connections to the Arctic Oscillation and the ENSO. *Geophysical Research Letters*, *31*, L09211. https://doi.org/10.1029/2004GL019858

Mann, M. E., Rahmstorf, S., Kornhuber, K., Steinman, B. A., Miller, S. K., & Coumou, D. (2017). Influence of anthropogenic climate change on planetary wave resonance and extreme weather events. *Scientific Reports*, *7*(1). https://doi.org/10.1038/srep45242

Markus, T., Stroeve, J. C., & Miller, J. (2009). Recent changes in Arctic sea ice melt onset, freezeup, and melt season length. *Journal of Geophysical Research*, *114*, C12024. https://doi.org/10.1029/2009JC005436

McKenna, C. M., Bracegirdle, T. J., Shuckburgh, E. F., Haynes, P. H., & Joshi, M. M. (2018). Arctic sea ice loss in different regions leads to contrasting Northern Hemisphere impacts. *Geophysical Research Letters*, *45*, 945–954. https://doi.org/10.1002/2017GL076433

Melillo, J. M., Richmond, T. C., & Yohe, G. W. (Eds) (2014). Climate change impacts in the United States. In *The Third National Climate Assessment* (p. 841). District of Columbia, USA: U.S. Global Change Research Program. District of Columbia. USA. https://doi.org/10.7930/J0Z31WJ2.

Mesinger, F., DiMego, G., Kalnay, E., Mitchell, K., Shafran, P. C., Ebisuzaki, W., et al. (2006). The North American regional reanalysis. *Bulletin of the American Meteorological Society*, *87*(3), 343–360. https://doi.org/10.1175/BAMS-87-3-343

Mitchell, D., Heaviside, C., Vardoulakis, S., Huntingford, C., Masato, G., P Guillod, B., et al. (2016). Attributing human mortality during extreme heat waves to anthropogenic climate change. *Environmental Research Letters*, *11*(7). https://doi.org/10.1088/1748-9326/11/7/074006

Mueller, B., & Seneviratne, S. I. (2012). Hot days induced by precipitation deficits at the global scale. *PNAS*, *109*(31), 12,398–12,403. https://doi.org/10.1073/pnas.1204330109

Nairn, J., Fawcett, R., & Ray, D. (2009). Defining and predicting excessive heat events, a National system. CAWCR Modeling Workshop, 30, 83-86.

Ogi, M., Barber, D. G., & Rysgaard, S. (2016). The relationship between summer sea ice extent in Hudson Bay and the Arctic Ocean via the atmospheric circulation. *Atmospheric Science Letters*, *17*(11), 603–609. https://doi.org/10.1002/asl.709

Osborne, J. M., Screen, J. A., & Collins, M. (2017). Ocean-atmosphere state dependence of the atmospheric response to Arctic sea ice loss. *Journal of Climate*, *30*(5), 1537–1552. https://doi.org/10.1175/JCLI-D-16-0531.1

Oswald, E. M., & Rood, R. B. (2014). A trend analysis of the 1930–2010 extreme heat events in the continental United States. *Journal of Applied Meteorology and Climatology*, *53*(3), 565–582. https://doi.org/10.1175/JAMC-D-13-071.1

Overland, J. E. (2016). A difficult Arctic science issue: Midlatitude weather linkages. *Polar Science*, *10*(3), 210–216. https://doi.org/10.1016/j.polar.2016.04.011

Overland, J. E., Dethloff, K., Francis, J. A., Hall, R. J., Hanna, E., Kim, S.-J., et al. (2016). Nonlinear response of mid-latitude weather to the changing Arctic. *Nature Climate Change*, *6*(11), 992–999. https://doi.org/10.1038/nclimate3121

Overland, J. E., & Wang, M. (2018). Arctic-midlatitude weather linkages in North America. *Polar Science*, *16*, 1–9. https://doi.org/10.1016/j.polar.2018.02.001

Pal, J. S., & Eltahir, E. A. B. (2016). Future temperature in southwest Asia projected to exceed a threshold for human adaptability. *Nature Climate Change*, *6*(2), 197–200. https://doi.org/10.1038/nclimate2833

Parkinson, C. L., & Cavalieri, D. J. (2008). Arctic sea ice variability and trends, 1979-2006. *Journal of Geophysical Research*, *113*, C07003. https://doi.org/10.1029/2007JC004558

Peng, G., & Meier, W. N. (2017). Temporal and regional variability of Arctic sea-ice coverage from satellite data. *Annals of Glaciology*, *59*(76pt2), 191–200. https://doi.org/10.1017/aog.2017.32

Perkins, S. E., Alexander, L. V., & Nairn, J. R. (2012). Increasing frequency, intensity, and duration of observed global heat waves and warm spells. *Geophysical Research Letters*, *39*, L20714. https://doi.org/10.1029/2012GL053361

Petoukhov, V., Rahmstorf, S., Petri, S., & Schellnhuber, H. J. (2013). Quasiresonant amplification of planetary waves and recent Northern Hemisphere weather extremes. *Proceedings of the National Academy of Sciences of the United States of America*, *110*(14), 5336–5341. https://doi.org/10.1073/pnas.1222000110

Pielke, R. A., Davey, C., & Morgan, J. (2004). Assessing "global warming" with surface heat content. *Eos, Transactions American Geophysical Union*, *85*(21), 210–211. https://doi.org/10.1029/2004EO210004

Piticar, A., Croitoru, A., Ciupertea, F., & Harpa, G. (2017). Recent changes in heat waves and cold waves detected based on excess heat factor and excess cold factor in Romania. *International Journal of Climatology*, *38*(4), 1777–1793. https://doi.org/10.1002/joc.5295

Qian, M., Jones, C., Laprise, R., & Caya, D. (2008). The influences of NAO and the Hudson Bay sea-ice on the climate of eastern Canada. *Climate Dynamics*, *31*(2-3), 169–182. https://doi.org/10.1007/s00382-007-0343-9

Rohini, P., Rajeevan, M., & Srivastava, A. K. (2016). On the variability and increasing trends of heat waves over India. *Scientific Reports*, *6*(1). https://doi.org/10.1038/srep26153

Russo, S., Dosio, A., Graversen, R. G., Sillmann, J., Carrao, H., Dunbar, M. B., et al. (2014). Magnitude of extreme heat waves in present climate and their projection in a warming world. *Journal of Geophysical Research: Atmospheres*, *119*, 12,500–12,512. https://doi.org/10.1002/2014JD022098

Schär, C. (2016). Climate extremes: The worst heat waves to come. *Nature Climate Change*, *6*(2), 128–129. https://doi.org/10.1038/nclimate2864

Schoof, J. T., Ford, T. W., & Pryor, S. C. (2017). Recent changes in U.S. regional heat wave characteristics in observations and reanalyses. *Journal of Applied Meteorology and Climatology*, *56*(9), 2621–2636. https://doi.org/10.1175/JAMC-D-16-0393.1

Schoof, J. T., Heern, Z. A., Therrell, M. D., & Remo, J. W. F. (2015). Assessing trends in lower tropospheric heat content in the central United States using equivalent temperature. *International Journal of Climatology*, *35*(10), 2828–2836. https://doi.org/10.1002/joc.4175

Schubert, S., Wang, H., & Suarez, M. (2011). Warm season subseasonal variability and climate extremes in the Northern Hemisphere: The role of stationary Rossby waves. *Journal of Climate*, *24*(18), 4773–4792. https://doi.org/10.1175/JCLI-D-10-05035.1

Schweiger, A., & Lindsay, R. (2015). Arctic sea ice thickness loss determined using subsurface, aircraft, and satellite observations. *The Cryosphere*, *9*(1), 269–283. https://doi.org/10.5194/tc-9-269-2015

Schweiger, A., Lindsay, R., Zhang, J., Steele, M., Stern, H., & Kwok, R. (2011). Uncertainty in modeled Arctic sea ice volume. *Journal of Geophysical Research*, *116*, C00D06. https://doi.org/10.1029/2011JC007084

Screen, J. A. (2017). Simulated atmospheric response to regional and pan-Arctic sea ice loss. *Journal of Climate*, *30*(11), 3945–3962. https://doi.org/10.1175/JCLI-D-16-0197.1

Screen, J. A., Deser, C., & Sun, L. (2015). Projected changes in regional climate extremes arising from Arctic sea ice loss. *Environmental Research Letters*, *10*(8). https://doi.org.10.1088/1748-9326/10/8/084006

Screen, J. A., & Francis, J. A. (2016). Contribution of sea-ice loss to Arctic amplification is regulated by Pacific Ocean decadal variability. *Nature Climate Change*, *6*(9), 856–860. https://doi.org/10.1038/nclimate3011

Screen, J. A., & Simmonds, I. (2010). The central role of diminishing sea ice in recent Arctic temperature amplification. *Nature*, *464*(7293), 1334–1337. https://doi.org/10.1038/nature09051

Screen, J. A., & Simmonds, I. (2014). Amplified mid-latitude planetary waves favor particular regional weather extremes. *Nature Climate Change*, *4*(8), 704–709. https://doi.org/10.1038/nclimate2271

Serreze, M. C., & Stroeve, J. (2015). Arctic sea ice trends, variability, and implications for seasonal ice forecasting. *Philosophical Transactions of the Royal Society A*, *373*(2045), 20140159. https://doi.org/10.1098/rsta.2014.0159

Shepherd, T. G. (2016). Effects of a warming Arctic. *Science*, *353*(6303), 989–990. https://doi.org/10.1126/science.aag2349

Tang, Q., Zhang, X., & Francis, J. A. (2014). Extreme summer weather in northern mid-latitudes linked to vanishing cryosphere. *Nature Climate Change*, *4*(1), 45–50. https://doi.org/10.1038/nclimate2065

Tang, Q., Zhang, X., Yang, X., & Francis, J. A. (2013). Cold winter extremes in northern continents linked to Arctic sea ice loss. *Environmental Research Letters*, *8*. https://doi.org/10.1088/1748-9326/8/014036

Tedesco, M., Mote, T., Fettweis, X., Hanna, E., Jeyaratnam, J., Booth, J. F., et al. (2016). Arctic cut-off high drives the poleward shift of a new Greenland melting record. *Nature Communications*, *7*(1), 11723. https://doi.org/10.1038/ncomms11723

Tivy, A., Howell, S. E. L., Alt, B., McCourt, S., Chagnon, R., Crocker, G., et al. (2011). Trends and variability in summer sea ice cover in the Canadian Arctic based on the Canadian Ice Service Digital Archive, 1960-2008 and 1968-2008. *Journal of Geophysical Research*, *116*, C03007. https://doi.org/10.1029/2009JC005855

Vihma, T. (2014). Effects of Arctic sea ice decline on weather and climate: A review. *Surveys in Geophysics*, *35*(5), 1175–1214. https://doi.org/10.1007/s10712-014-9284-0

Walsh, J. E. (2014). Intensified warming of the Arctic: Causes and impacts on middle latitudes. *Global and Planetary Change*, *117*, 52–63. https://doi.org/10.1016/j.gloplacha.2014.03.003

Wang, J., Mysak, A. L. A., & Ingram, R. G. (1994). Interannual variability of sea-ice cover in Hudson Bay, Baffin Bay and the Labrador Sea. *Atmosphere-Ocean*, *32*(2), 421–447. https://doi.org/10.1080/07055900.1994.9649505

Xia, Y., Mitchell, K., Ek, M., Sheffield, J., Cosgrove, B., Wood, E., et al. (2012). Continental-scale water and energy flux analysis and validation for the North American Land Data Assimilation System program phase 2 (NLDAS-2): 1. Intercomparison and application of model products. *Journal of Geophysical Research*, *117*, D03109. https://doi.org/10.1029/2011JD016048